CSIRO PUBLISHING

International Journal of Wildland Fire **2018**, *27*, 498–499
https://doi.org/10.1071/WF17113_CO

Corrigendum

Corrigendum to: Use of ordinary kriging and Gaussian conditional simulation to interpolate airborne fire radiative energy density estimates

C. Klauberg, A. T. Hudak, B. C. Bright, L. Boschetti, M. B. Dickinson, R. L. Kremens and C. A. Silva

International Journal of Wildland Fire **27**, 228–240. https://doi.org/10.1071/WF17113

The authors of the above mentioned paper regret that there were errors in Figures 2 and 7. The all-terrain vehicle (ATV) ignition lines depicted in Fig. 7*a* were missing the ignition line along the southeastern boundary of the L2F block, which was where the prescribed burn at L2F was initially lit. The omission has since been corrected in the cited data archive product (Hudak *et al.* 2017). Moreover, the ignition lines should not have been shown in Fig. 7, which was otherwise correct, but should have been in Fig. 2 in association with the number of Fire Radiative Power Density (FRPD) observations, as was stated in the Fig. 2 caption of the original paper. Corrected Figures 2 and 7 are provided below.

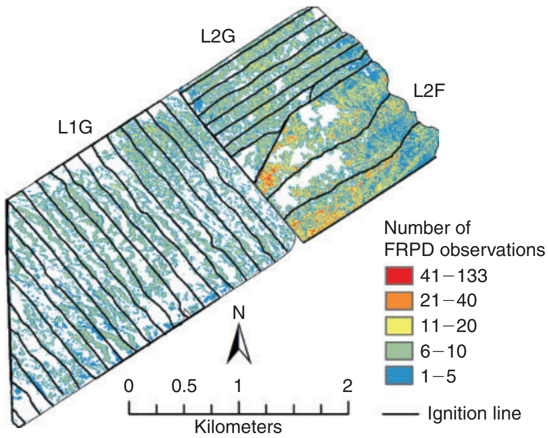

Fig. 2. Number of fire radiative power density (FRPD) observations recorded by the airborne Wildland Airborne Sensor Program (WASP) instrument per active fire pixel while imaging the 2012 burn blocks. Overlaid are the all-terrain vehicxle (ATV) ignition lines (Hudak *et al.* 2017).

Journal compilation © IAWF 2018

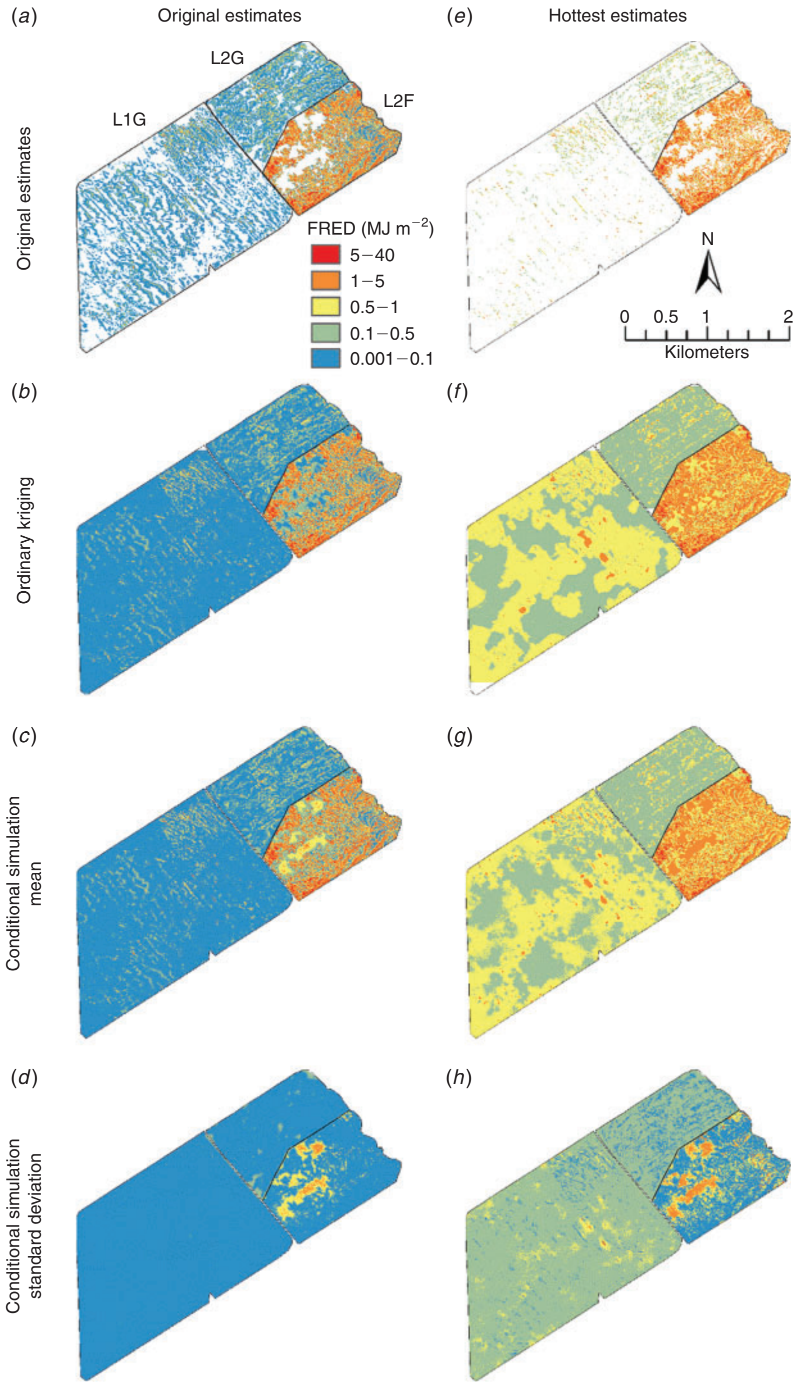

Fig. 7. Original uninterpolated (*a*, *e*), ordinary kriging (OK) interpolated (*b*, *f*), and Gaussian conditional simulation (GCS) interpolated (*c*, *d*, *g*, *h*) fire radiative energy density (FRED) maps of the 2012 burn blocks (L1G, L2G, L2F). Maps based on original FRED estimates are shown in the left column (*a*, *b*, *c*, *d*); maps based on hottest FRED estimates are shown in the right column (*e*, *f*, *g*, *h*).

Reference

Hudak, A.T., B.C. Bright, B.W. Williams, and Hiers, J. K. (2017). RxCADRE 2011 and 2012: Ignition data. Fort Collins, CO: Forest Service Research Data Archive. Updated 31 May 2018. https://doi.org/10.2737/RDS-2017-0065

CSIRO PUBLISHING

International Journal of Wildland Fire **2018**, *27*, 228–240
https://doi.org/10.1071/WF17113

Use of ordinary kriging and Gaussian conditional simulation to interpolate airborne fire radiative energy density estimates

C. Klauberg[A], *A. T. Hudak*[A,E], *B. C. Bright*[A], *L. Boschetti*[B], *M. B. Dickinson*[C], *R. L. Kremens*[D] *and C. A. Silva*[B]

[A]USDA Forest Service Rocky Mountain Station, Forestry Sciences Laboratory, 1221 South Main Street, Moscow, ID 83843, USA.
[B]University of Idaho, 708 South Deakin Street, Moscow, ID 83844, USA.
[C]USDA Forest Service, Northern Research Station, 359 Main Road, Delaware, OH 43015, USA.
[D]Rochester Institute of Technology, Center of Imaging Science, 54 Lomb Memorial Drive, Rochester, NY 14623, USA.
[E]Corresponding author. Email: ahudak@fs.fed.us

Abstract. Fire radiative energy density (FRED, J m^{-2}) integrated from fire radiative power density (FRPD, W m^{-2}) observations of landscape-level fires can present an undersampling problem when collected from fixed-wing aircraft. In the present study, the aircraft made multiple passes over the fire at ~3 min intervals, thus failing to observe most of the FRPD emitted as the flame front spread. We integrated the sparse FRPD time series to obtain pixel-level FRED estimates, and subsequently applied ordinary kriging (OK) and Gaussian conditional simulation (GCS) to interpolate across data voids caused by the undersampling. We compared FRED interpolated via OK and GCS with FRED estimated independently from ground measurements of biomass consumed from five prescribed burns at Eglin Air Force Base, Florida, USA. In four of five burns considered where undersampling prevailed, OK and GCS effectively interpolated FRED estimates across the data voids, improving the spatial distribution of FRED across the burning event and its overall mean. In a fifth burn, the burning characteristics were such that undersampling did not present a problem needing to be fixed. We also determined where burning and FRPD sampling characteristics merited applying OK and CGS only to the highest FRED estimates to interpolate more accurate FRED maps.

Additional keywords: fire behaviour, fire modeling, fire modelling, fire radiative energy, remote sensing, RxCADRE.

Received 29 July 2017, accepted 17 February 2018, published online 23 April 2018

Introduction

Biomass burning is one of the main sources of greenhouse gas emissions in the atmosphere (Seiler and Crutzen 1980; Bowman *et al.* 2009). In particular, many of the trace gases emitted by burning vegetation have oxidising components, and the organic carbon and carbon black aerosols scatter and absorb solar radiation respectively (Andreae 1991; Jacobson 2001). The combination of these compounds with electromagnetic radiation, added to changes in land surface properties, can cause changes in radiation balance, biogeochemical cycles and cloud nucleation (Kaufman *et al.* 1990). Quantification of fuel stocks and fuel consumption, and the emission of gases and aerosols to the atmosphere, are important issues for the fire science community and government agencies.

Burning biomass during wildland fire generates radiative heat measurable remotely and quantified as fire radiative power (FRP; W), which can be integrated over time to estimate fire radiative energy (FRE; J). FRP and FRE are linearly related to biomass combustion rate and biomass combusted respectively (Wooster *et al.* 2003; Ellicott *et al.* 2009; Freeborn *et al.* 2011; Kremens *et al.* 2012; Smith *et al.* 2013; Hudak *et al.* 2016*b*). As a consequence, fire energy estimations can support large-area estimations of biomass burned (Roberts *et al.* 2011) and atmospheric emissions (Kaiser *et al.* 2012), and at the local level supply important information to fire management plans, fire and smoke models and measurement methods (Ottmar *et al.* 2016*a*).

Owing to the large extent of wildland burned areas and the feasibility of collecting radiative power measurements remotely over a range of spatial and temporal scales, remote sensing may be the most viable tool in monitoring wildland fires and FRE across time and space (Wooster *et al.* 2003). Satellite and high-resolution aerial imagery has been used to monitor fires over large and small areas at high resolution (Riggan *et al.* 2004; Roberts and Wooster 2008). Remote sensing techniques have been applied for detection, mapping and quantification of biomass burned, FRP, FRE and atmospheric emissions

Journal compilation © IAWF 2018

(Van Der Werf *et al.* 2003; Smith and Wooster 2005; Roberts and Wooster 2008; Boschetti and Roy 2009; Ellicott *et al.* 2009; Kaiser *et al.* 2012; Strand *et al.* 2016).

Remote sensing at mid-wave infrared (MWIR) and long-wave infrared (LWIR) wavelengths provides excellent opportunities for estimating FRP via the dual-band technique (Dozier 1981). The Moderate-Resolution Imaging Spectroradiometer (MODIS) sensor (1-km resolution) onboard EOS-Terra and Aqua, Visible Infrared Imaging Radiometer Suite (VIIRS) (375-m resolution) and other polar-orbiting satellites are capable of detecting active fires and estimating FRP only twice daily (Giglio *et al.* 2003; Schroeder *et al.* 2014), making them highly affected by temporal undersampling. The latest generation of geostationary satellites, such as Meteosat Second Generation (MSG), the recent GOES-R (launched by NOAA-NASA November 2016) and Himawari-8 (launched by the Japan Meteorological Agency October 2014) have potential for near-real-time fire monitoring, but with lower spatial resolution than polar-orbiting satellites: 3 km at nadir for MSG, 2 km for GOES-R and Himawari-8.

Undersampling is a major issue affecting the accuracy of FRE retrievals from MODIS FRP observations, and from polar orbiting sensors in general (Boschetti and Roy 2009; Kumar *et al.* 2011). Boschetti and Roy (2009) observed that the acquisition constraints imposed by the satellite sensing and orbit geometry, clouds and active fire product omission errors resulted in undersampling both in the spatial and temporal domain, and that the straightforward linear integration of FRP observations through time resulted in a systematic underestimation of energy release and consequently of biomass consumed. Ordinary kriging was found to be an effective way of compensating for MODIS temporal oversampling.

Continuous imaging of active fires over large areas at high spatial resolution has remained a challenge, though unmanned aerial vehicles (UAV) with suitable imaging systems may offer opportunities for modest-sized fires (Zajkowski *et al.* 2016). Moving aerial platforms without hovering capability, such as fixed-wing aircraft, have more flexibility than spacecraft to collect repeated observations over the full duration of a typical fire, but nonetheless collect only a sparse sample of FRP over time. Albeit more frequent than the sampling provided by satellite systems, the temporal sampling of aircraft observations negatively affects the estimation of FRE whenever part of the fire spread is missed. Hudak *et al.* (2016*b*) produced landscape-level FRE maps from repeated airborne FRP observations. Issues with spatial and temporal undersampling; however, remained: with a fast-moving flame front, each location was actively burning only for a limited time. In some locations, the aircraft failed to acquire any measurements while the fire was actively burning, resulting in gaps in the FRE map. As a consequence, Hudak *et al.* (2016*b*) suggested that kriging might also be needed when retrieving FRE from airborne high-resolution observations.

Spatial variation in fire radiative flux may occur owing to small changes of both wind direction and speed frequently altering the fire spread (Clements *et al.* 2016), and owing to heterogeneously distributed fuel (Hudak *et al.* 2016*b*). Various statistical methods can be used to interpolate a value at an unobserved location from observations at nearby locations while accounting for local spatial variability, such as kriging and other geostatistical methods (Journel and Huijbregts 1978). An advantage of geostatistical techniques is the ability to evaluate the uncertainty of the predicted response (FRE, in our case). Ordinary kriging (OK), as a geostatistical data interpolation method, uses the spatial dependency between neighbouring samples to estimate values at any position within the analysis space, to which the semivariogram model is fitted, without anisotropy and with minimum variance (Journel and Huijbregts 1978; Goovaerts 1997). Spatial dependency could be evaluated by a spatial dependency model that provides parameters to estimate the response at unsampled places (Goovaerts 1997). OK has been widely used, for example, for mapping forest canopy height (Hudak *et al.* 2002), cork and pine resin production (Nanos *et al.* 2001; Montes *et al.* 2005), and lightning-caused wildfires (Ordóñez *et al.* 2012).

However, kriging methods have some disadvantages: interpolated surfaces are smoothed, and can potentially be biased, with underestimation and overestimation of the response variable. An alternative geostatistical method is Gaussian simulation, which preserves the spatial characteristics and variance of the sample data; moreover, Gaussian conditional simulation (GCS) honours the measured values at the sampled locations (as opposed to 'unconditional' simulation) (Andriotti 2004). Berterretche *et al.* (2005) used GCS to estimate leaf area index across a boreal forest. Haywood (2006) used GCS to estimate distribution and abundance of blackbutt (*Eucalyptus pilularis* Sm.). Wei and Shao (2009) conducted a study using GCS to verify the spatial variability of soil pH values in a small watershed.

In this context, our study aims to use OK and GCS to interpolate FRE estimates separated by data voids that are an artefact of undersampling of FRP across a burn area. We assumed that the fire spread rate and FRP varied independently from the timing and frequency of the image collection, such that the FRP time series constituted an unbiased sampling of the fire activity. By extension, similar implementation of geostatistical interpolation or simulation methods more broadly to satellite FRP products could have useful implications for mapping and management of carbon pools (fuels) and fluxes (gas and particulate emissions), with associated impacts on air quality at regional and global scales, that contribute to greenhouse gases and carbon balance.

Materials and methods

Study area and prescribed fires

The study was conducted over five prescribed burns (henceforth, 'burn blocks') performed at Eglin Air Force Base (AFB) located in the Florida panhandle (USA), during the Prescribed Fire Combustion and Atmospheric Dynamics Research Experiment (RxCADRE) in 2011 and 2012 (Ottmar *et al.* 2016*a*). Elevations range from 52 to 85 m with flat topography and deep, well-drained sandy deposits of Quartzipsamments of the Lakeland series. Mean annual precipitation is 158 cm and mean annual temperature is 19.8°C (Overing *et al.* 1995). Most forested areas are dominated by longleaf pine (*Pinus palustris* Mill.) maintained by Eglin AFB managers, with frequent fires prescribed typically at 1–3 year intervals and recorded since 1972 in a geodatabase.

Table 1. Description of the prescribed burn blocks at Eglin Air Force Base
Sources: adapted from Ottmar *et al.* (2016*a*, 2016*b*) and Hudak *et al.* (2016*b*)

Burn block	Area (ha)	Burn date	Surface fuel load (Mg ha^{-1})	Fuel consumption (Mg ha^{-1})	Relative consumption (%)	Fuel water content (%)	Mean overstorey canopy cover (%)
703C	668	6-Feb-11	5.35	3.03	56.5	21.2	25
608A	828	8-Feb-11	5.97	4.68	79.1	17.6	22.7
L1G	454	4-Nov-12	2.15	1.54	72.7	43.9	0
L2G	127	10-Nov-12	3.57	3.09	85.3	33.8	0
L2F	151	11-Nov-12	10.8	6.36	58.9	17.8	37.3

Five land-management blocks were selected for burning, which followed operational prescribed burning protocols used at Eglin AFB. The 2011 burn blocks (703C and 608A) were ignited with incendiary spheres deployed from a helicopter, whereas the 2012 burn blocks (L1G, L2G and L2F) were ignited from all-terrain vehicles on which were mounted drip torches. By either method, the strategy was to lay firelines in parallel strips to produce heading or flanking fire.

Fuels

Three burn blocks were forested (703C, 608A and L2F) whereas two were non-forested (L1G and L2G) (Table 1). Surface fuel beds in the non-forested units comprised variable proportions of litter, grasses, forbs and shrubs dominated by Turkey oak (*Quercus cerris* L.), whereas surface fuel beds in the forested units comprised the same materials plus longleaf pine needle cast and some woody debris (Ottmar *et al.* 2016*b*). Fuel accumulations since the previous burn were 23 months at 703C and 608A, 12 months at L1G, and 19 or 31 months at L2G and L2F, depending on the locality.

Shrub, herbaceous (forbs, grass and needles), litter and woody debris were measured both pre- and post-fire in separate 1 m^2 (burn blocks besides L2F) or 0.25 m^2 (L2F) destructive harvest (clip) plots; ovendry weights of each component were summed to calculate total surface fuel load, as described in Ottmar *et al.* (2016*b*). Fuel consumption (Table 1) was estimated for each burn block as the difference in measured fuel loads between equal numbers of pre- and post-fire clip plots; from these calculations of fuel consumption (FC, kg m^{-2}), expected values of fire radiative energy density ($FRED_{exp}$) were calculated using three published linear relationships between FC and FRE, all based on small-fire experiments conducted under different conditions. Wooster *et al.* (2005), burning outdoors, combusted 15 fuel beds of *Miscanthus* grasses dried to ~12% gravimetric moisture content. Freeborn *et al.* (2008) assembled 44 fuel beds collected across a broad range of fuel types, which were oven-dried, reassembled and burned in a combustion chamber. Smith *et al.* (2013) explicitly explored effects of fuel moisture in a combustion laboratory, burning 24 fuel beds of *Pinus monticola* Douglas ex D.Don (western white pine) needles while varying fuel gravimetric water content (*Wc*, %) from 1 to 14%. Unlike Wooster *et al.* (2005) and Freeborn *et al.* (2008), Smith *et al.* (2013) did not force the simple linear regression model intercept through the origin when formulating the linear relationship between FRE and FC. In the present study, *Wc* was calculated from day-of-burn fuel moisture measurements reported by Ottmar *et al.* (2016*b*) for litter, herbaceous (grasses and forbs), shrubs (including oaks), and woody fuels; the overall mean *Wc* was weighted by consumption estimates also reported by Ottmar *et al.* (2016*b*) for each of these four fuel components in each burn block.

Wildfire Airborne Sensor Program (WASP) LWIR image acquisition and processing

The Wildfire Airborne Sensor Program (WASP) system (McKeown *et al.* 2004; Ononye *et al.* 2007) was mounted on board a twin-engine Piper Navajo that flew over the burn blocks at ~3-min intervals to image the active fires on the dates recorded in Table 1. The WASP LWIR sensor has an 8–9.2 μm bandwidth, and in this study, spatial resolution of 1.5–3 m and spatial extent of 0.9–1.9 km (Dickinson *et al.* 2016). WASP LWIR digital numbers were calibrated to at-sensor radiance (W m^{-2} sr^{-1}) and then used to estimate fire radiative power density (FRPD, W m^{-2}) (Dickinson and Kremens 2016). Active fire pixels were differentiated from ambient pixels using a FRPD threshold of 1070 W m^{-2}, which was determined independently from nadir-viewing, ground-based radiometers ($n = 60$) distributed across the burn blocks (Hudak *et al.* 2016*b*). At each active fire pixel, the FRED was calculated from the FRPD time series, with FRED estimated ($FRED_{est}$) (J m^{-2}) for each fire pixel using the trapezoidal rule for numerical integration by Eqn 1, following Boschetti and Roy (2009):

$$FRED_{est} = \sum_{i}^{n} 0.5(FRPD_i + FRPD_{i-1})(t_i - t_{i-1}) \quad (1)$$

where $FRPD_i$ is the *i*th FRPD observation in the time series, and t_i is its acquisition time expressed in seconds (s), starting from the first observation. Pixels with <4 FRPD measurements were assumed to have a fire rate of spread of 0.25 m s^{-1}, as reported by Butler *et al.* (2016) for the L2G burn block, which conveniently had the median fuel consumption of the five burn blocks considered. Although images were collected every 3 or 4 s within an overpass, ~3 min would elapse between overpasses (Dickinson *et al.* 2016, Hudak *et al.* 2016*b*), resulting in temporal undersampling (Fig. 1*a*). Spatial undersampling also occurred in that the spatial extent of the image frames was smaller than the burn blocks, especially for the larger 703C and 608A blocks burned in 2011 (Fig. 1*b*). Temporal and spatial undersampling effectively reduced the number of FRPD observations collected per pixel (Fig 2 and Fig. S1, available as Supplementary Material to this paper).

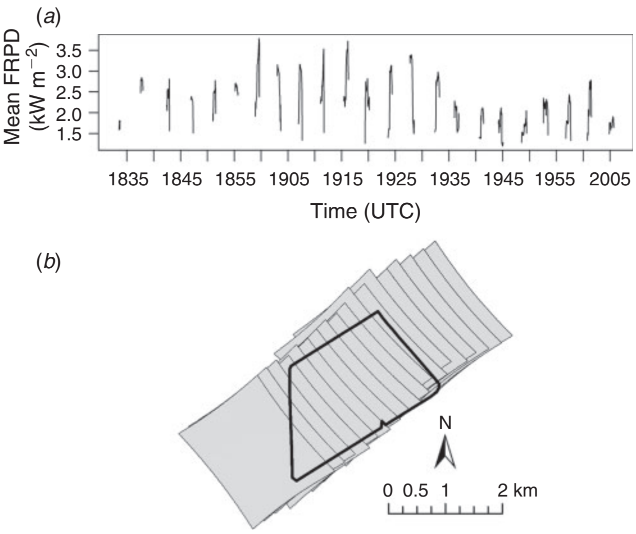

Fig. 1. (*a*) Time series of mean fire radiative power density (FRPD) for burn block L1G. Breaks in the FRPD time series, when the airborne sensor was not collecting imagery over the fire, illustrate temporal undersampling. (*b*) Burn block L1G (bold outline) and overlapping WASP image frames (solid grey squares) from one plane overpass. Many frames imaged every 3 s did not completely cover burn extents, illustrating spatial undersampling. Abbreviation: UTC: Universal Time Co-ordinated.

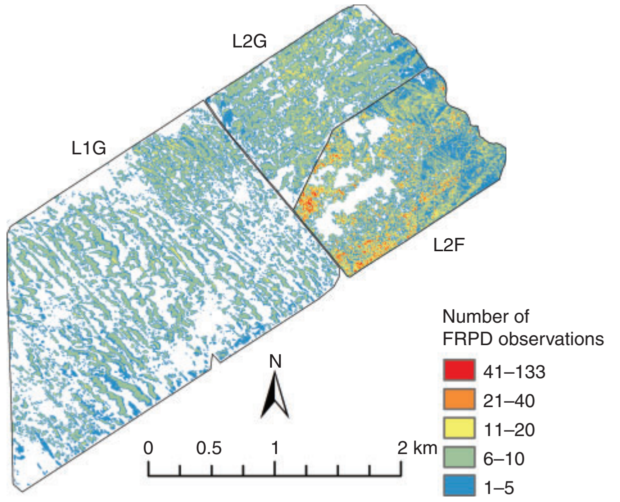

Fig. 2. Number of fire radiative power density (FRPD) observations recorded by the airborne Wildland Airborne Sensor Program (WASP) instrument per active fire pixel while imaging the 2012 burn blocks. Overlaid are the all-terrain vehicle (ATV) ignition lines (Hudak *et al.* 2017).

Canopy cover in the three forested blocks (Table 1) was calculated at the pixel level from airborne LiDAR returns collected at a nominal point density of 7 m^{-2} (Hudak *et al.* 2015*b*, 2016*b*). Mitigation of the FRPD signal from these surface fires due to occlusion by the overstorey trees in the three forested blocks was assumed to be in proportion to overstorey canopy cover (Mathews *et al.* 2016), so the FRPD estimate at each pixel was increased by the canopy cover proportion (Hudak *et al.* 2016*a*, 2016*b*).

Data transformation

The transformation and back-transformation method used in this study was chosen based on the characteristics of the lognormal FRED data distribution, characterised by positive skewness where the mean is greater than the median of the distribution (see Supplementary Material). The goal of the lognormal transformation is to have a more or less normalised frequency distribution, instead of a skewed distribution (Yamamoto 2005). The variance of the data is reduced by normalisation, which means that the calculation of statistics (weighted averages and OK estimates) is improved (Goovaerts 1997; Yamamoto 2005, 2010). The lognormal kriging is the geostatistical estimator based on a logarithmic transformation. This estimator takes advantage of a transformed data distribution, reducing the influence of a few high values on the model (Yamamoto and Furuie 2010). Without data transformation, low values are overestimated and high values are underestimated (Yamamoto 2010).

It is necessary to return the transformed lognormal kriging estimates back to the original measurement scale, but the back-transformation itself introduces a bias. Several authors have proposed alternative approaches for transformation and back-transformation (Journel 1980; Yamamoto 2005; 2007; 2010; Yamamoto and Furuie 2010), and after some tests with the study dataset and equations, the equations proposed by Yamamoto (2010) (Eqns S1*a*, S1*b*) and Papritz and Schwierz (2016) (Eqns S2*a*, S2*b*) were combined (Eqns 2*a*, 2*b*).

$$\mathrm{FRED}_{\mathrm{transf}} = \ln(\mathrm{FRED}_{\mathrm{est}}/median_{\mathrm{FREDest}}) \tag{2a}$$

$$\mathrm{FRED}_{\mathrm{back\ transf}} = \exp\big(\mathrm{FRED}_{\mathrm{pre}} + 0.5 \times \left(variance_{\mathrm{FREDtransf}} - variance_{\mathrm{FREDpre}}\right)\big) \times median_{\mathrm{FREDest}} \tag{2b}$$

where $\mathrm{FRED}_{\mathrm{est}}$ is the input value (observed value) and $\mathrm{FRED}_{\mathrm{pre}}$ is the predicted value after OK or GCS.

Hottest pixel subset

The $\mathrm{FRED}_{\mathrm{est}}$ values were transformed with Eqn 2*a*. Examining histograms of transformed FRED rasters revealed trimodal distributions for each burn block, when in theory the transformed distributional shapes should be unimodal if not for undersampling (Fig. 3). We assumed the hottest pixels, those of the rightmost peak with the greatest recorded energy release, to be those unaffected, or least affected, by undersampling bias. For each burn block, we used the low value between the middle and rightmost peaks of the histogram as an objective criterion for defining a 'hottest' pixel threshold, back-transformed that threshold (Eqn 2*b*) and dropped values below the back-transformed threshold in the original FRED rasters to produce new rasters of just the hottest pixels. OK and GCS were performed on hottest FRED rasters that represented where more FRPD observations happened to be captured, in addition to being performed on the original FRED rasters.

Ordinary kriging

OK was performed with the Spatial Analyst Tools extension of ArcGIS 10.2 (ESRI, Redlands, CA, USA), which automatically

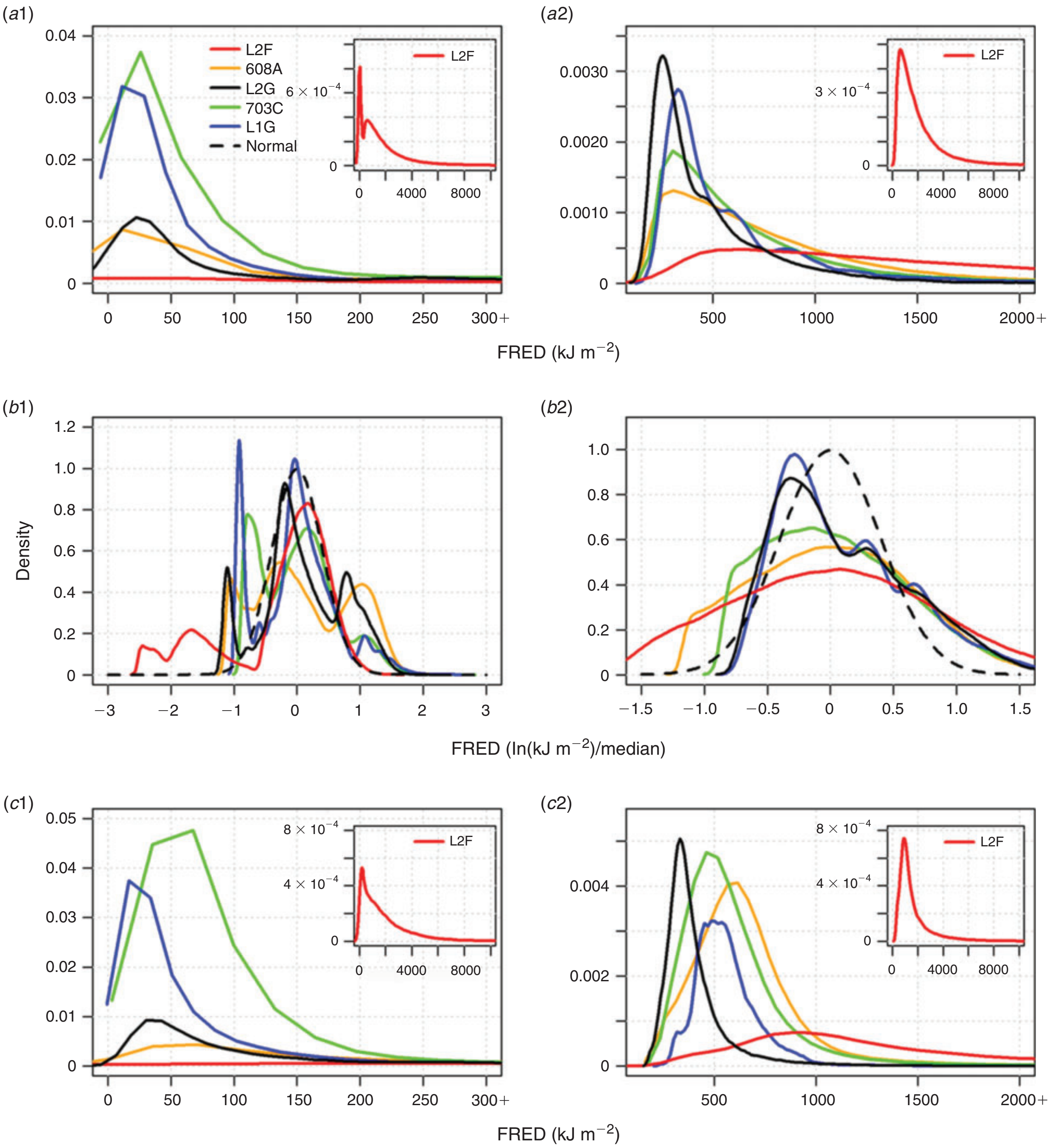

Fig. 3. Density distribution for (*a*) original fire radiative energy density (FRED) (kJ m^{-2}) data; (*b*) transformed FRED ((ln(kJ m^{-2}) per median) data; and (*c*) the back-transformed values after ordinary kriging (OK) to all FRED pixels (left) and hottest FRED pixels dataset (right). A normal distribution, represented by the dotted line (*b*), is provided for comparison with the transformed distributions at the five burn blocks. A broader view of FRED density at the L2F burn block, given its longer tail, is displayed in the inset graphs included (*a*, *c*).

fitted semivariograms and provided a map with predictions as a final product. Semivariograms were generated from the hot pixels in the final map to compare with the original hot pixel semivariograms. For fitting the experimental semivariograms, we tested the exponential, Gaussian and spherical models (see Supplementary Material).

To analyse the degree of spatial dependence of the attribute under study, we used the Spatial Dependence Index (SDI%), defined by Eqn 3:

$$\mathrm{SDI}(\%) = \frac{C_1}{C_0 + C_1} \times 100 \tag{3}$$

where $C_0 =$ nugget effect and $C_0 + C_1$ is the partial sill. Cambardella *et al.* (1994) classified SDI as follows: (i) SDI $< 25\%$, strong spatial dependence; (ii) $25\% < \text{SDI} < 75\%$, moderate spatial dependence; and (iii) SDI $> 75\%$, weak spatial dependence.

WASP pixel-based estimates of FRED were tested for anisotropy (a directional component) following Journel and Huijbregts (1978) and Wackernagel (2003).

Gaussian conditional simulation

GCS was performed with the geostatistical analyst tool in ArcGIS 10.2 (see Supplementary Material). Briefly, the steps used for the analysis are given by Andriotti (2004) as follows.

(1) The data distribution was transformed to normal: the sampled data were prepared using trend removal, declustering and normal score transformation.
(2) Simple kriging was applied, in which the semivariogram was estimated and search neighbourhood was defined.
(3) Conditioned simulations were performed to the observations 100 times: the simulation using the simple kriging raster was used as input, original data were used as a conditioner. The simulations were subsequently back-transformed to the natural scale.
(4) After the conditional simulation was applied, output rasters were generated cell by cell based on statistic type (mean, maximum and standard deviation) calculated across the 100 simulated rasters.

Accuracy assessment

Accuracy of interpolated FRED maps compared with the original FRED maps was tested using two independent ground datasets described by Hudak *et al.* (2016*b*). The first dataset was estimates of FRED integrated from 52 ground-based FRPD measurement instruments distributed across all five burn blocks at accurately surveyed instrument locations (Hudak *et al.* 2015*a*, 2016*c*). The field of view (FOV) varied between different nadir-viewing ground sensors: 5.5 m tower-based, dual-band radiometers with a 2.68 m-radius FOV ($n = 33$) (Dickinson *et al.* 2016); 8.2-m tripod-based radiometers with a 4.45 m radius FOV ($n = 9$); 8.2 m tripod-based LWIR cameras ($n = 10$) with either a 2.5×3.3 m FOV or a 4.8×6.4 m FOV (O'Brien *et al.* 2016). Given the range of instruments with different FOVs, and uncertainty over what portion of the FOV might include a WASP data void, we simply extracted the WASP pixel value at each instrument location, which was of survey-grade accuracy (Hudak *et al.* 2016*c*). The second dataset was expected values of FRED calculated from observed fuel consumption, estimated by multiplying percentage consumption observed at each burn block (Table 1) with pre-fire surface fuel load measurements collected at 279 destructive sample plots distributed across all five burn blocks by Ottmar and Restaino (2014), while also factoring in fuel water content (Table 1) as described in the preceding fuels section. We extracted WASP FRED pixel values at clip-plot centre locations, and assumed the effect of fuel removal from the 1×1-m (burn blocks besides L2F) or 0.5×0.5 m (L2F) clip plots had a negligible effect on the FRPD signal recorded by WASP at the 3×3 m (L1G and L2G), 2.8×2.8 m (703C), 2×2 m (608A) or 1.5×1.5 m (L2F) resolution of the WASP pixels. Using R (R Core Team 2015), paired Wilcoxon signed-rank and Spearman rank correlation tests were performed comparing WASP-derived estimates of FRED (original, hottest and interpolated) with both ground-based estimates of FRED.

Results

The FRED data in all study blocks were highly skewed and lognormally distributed. After natural log-transformation of the FRED data (Eqn 2*a*), models of the semivariance were fitted to the data that invariably displayed spatial autocorrelation. Exponential models were used in all OK as they better approximated the shape of the binned sample semivariograms than the spherical or Gaussian models also customarily considered. The SDI was <25% in all burn blocks, indicating strong spatial dependency (Table 2). Anisotropy was found to be negligible in all five burn blocks (Table 2).

Semivariogram range values did not show considerable variability among the blocks in the original FRED samples, ranging from 17 to 26 m (Table 2; Fig. 4), and in the hottest pixel dataset, ranging from 10 to 32 m. The average spatial lag in FRED values for all blocks was 21.44 ($\pm$2.86) m.

The nugget effect represents field and experimental variability, or random variability that is undetectable at the scale of sampling (Yamamoto and Landim 2013). Some nugget effect, as indicated by SDI (Table 2), was observed in two forested blocks (608A and L2F) when all pixels were considered, and may be due to obscuration of the FRED signal by the overstorey tree canopy (Hudak *et al.* 2016b), although the SDI was zero at the forested 703C block. Nevertheless, all burn blocks exhibited strong spatial dependency in FRED with SDI $< 25\%$ for both the all-pixels and hottest-pixels datasets (Table 2).

The data transformation reduced the data asymmetry to approximate a normal distribution before kriging. Transforming the FRED data distributions revealed trimodality in the FRED data from all five burn blocks (Fig. 3). The L1G block with the lowest fuel loads (Table 1) had the smallest third peak whereas the L2F block with the highest fuel loads (Table 1) had the largest third peak (Fig. 3). The L2G block was intermediate in this respect, with a transformed data distribution closest to normal (Fig. 3); accordingly, L2G had the smallest skewness statistic after natural log-transformation (all hot pixels dataset) (Table 2).

Higher FRED values were associated with greater fuel consumption (Table 1; Fig. 5). Summary statistics of OK FRED grids were generally comparable with those of GCS FRED grids for all as well as only the hottest estimates of FRED. Mean values of FRED grids interpolated from only the hottest pixels were closer to expected values of FRED at the 703C, 608A and L2G burn blocks (Fig. 5) based on observed surface loads for each block (Table 1), whereas at the L1G and L2F burn blocks, hottest OK and GCS interpolations of FRED exceeded expected FRED. Variability in FRED estimated and interpolated across these landscape-level burn blocks was much greater (particularly at L2F) than the 95% confidence intervals bounding expected FRED, because the latter were based on small-scale burn experiments of homogeneous fuel beds.

Paired Wilcoxon signed-rank tests showed that WASP-derived FRED estimates extracted from the OK and GCS grids

Table 2. Geostatistical and statistical parameters used for ordinary kriging (OK)
Abbreviation: SDI, Spatial Dependence Index

Parameters	703C	608A	L1G	L2G	L2F
General					
Model type	Exponential	Exponential	Exponential	Exponential	Exponential
Anisotropy	FALSE	FALSE	FALSE	FALSE	FALSE
Lag size	2.3	3	3.5	3	3
Number of lags	12	12	12	12	12
Number of points	75	75	75	75	75
Max. distance (m)	300	300	300	300	300
All pixels					
Nugget	0	0.08	0	0	0.07
Major range (m)	18.86	20.83	25.01	22.56	21.62
Partial sill	0.25	0.43	0.36	0.41	0.56
SDI (%)	0	18.30	0	0	12.07
Skewness (transformed data)	0.44	0.17	0.34	0.02	−1.07
Kurtosis (transformed data)	2.59	1.88	2.95	2.38	3.14
Hottest pixels					
Nugget	0	0	0	0	0
Major range (m)	27.6	10.39	31.93	17.28	16.12
Partial sill	0.38	0.36	0.28	0.27	0.59
SDI (%)	0	0	0	0	0
Skewness (transformed data)	0.70	0.24	0.91	0.67	0.20
Kurtosis (transformed data)	3.46	2.60	3.68	2.83	2.64

based on just the hottest pixels did not significantly differ from FRED observed independently at the ground-based sensors (Fig. 6). However, only the hottest, uninterpolated, WASP-derived FRED estimates did not significantly differ from independent, harvest fuel-derived expectations of FRED (Fig. S2). WASP-derived FRED estimates were better correlated with 52 ground-based FRED observations than with expected FRED based on harvested fuel observations (Figs 6, S2). Spearman correlations between WASP-estimated FRED and ground-measured FRED decreased following geostatistical interpolation (Fig. 6). Spearman correlations between WASP-derived FRED and harvest fuel-based expectations of FRED increased when all original FRED estimates were interpolated but decreased when just the hottest FRED estimates were interpolated (Fig. S2).

Discussion

These were all prescribed surface fires, but three of the five burn blocks considered were forested, where the tree canopy occluded the FRPD signal recorded by the WASP sensor on board the aircraft. Based on the finding of Mathews *et al.* (2016) that the fraction of FRP recorded at sensor varies linearly and in inverse proportion to canopy cover, Hudak *et al.* (2016*a*, 2016*b*) corrected for canopy occlusion by increasing the pixel-level FRPD value in proportion to the canopy cover proportion (Table 1). Although estimated FRED variance is higher in the three forested burn blocks (Fig. 5), so are the estimated FRED means, i.e. there is no clear trend in the coefficient of variation between the five burn blocks, regardless of interpolation procedure employed (or not), suggesting our canopy cover correction does not appear to have contributed to higher variance in estimated FRED. Nevertheless, this simple canopy cover correction does not account for the complex tree crown geometries as well as the variable sensor view angles that are both contributing to variability in FRED estimated from WASP. (Although airborne LiDAR data used by Hudak *et al.* (2016*a*, 2016*b*) for the canopy cover correction were collected from the same airplane as the WASP data, they were collected on different days and following different flight paths.)

The higher nugget effect in the 608A and L2F forested burn blocks could be attributable to higher fuel loads and fuel heterogeneity compared with the 703C forested and two non-forested blocks, as Ottmar *et al.* (2016*a*, 2016*b*) reported higher fuel load means (except for herbaceous fuels) and standard deviations in forested blocks than in non-forested blocks. Higher day-of-burn fuel water contents measured at L1G and (to a lesser extent) L2G (Table 1) are due to a higher proportion of herbaceous and live shrub fuels on these two non-forest blocks before the burns, compared with the three forested blocks. Higher fuel water content in L1G and L2G (Table 1) lowered expected FRED values per Smith *et al.* (2013) and likely contributed to lower estimated FRED (Fig. 5).

The predominant wind direction during the prescribed fires was recorded by ground crews in all burn blocks. At each burn block, we tested for anisotropy by using directional semivariograms conditioned on the wind direction, but what weak (if any) evidence we found for anisotropy was related not to the wind direction but to the spatial pattern of the ignition lines (Figs 7, S3, S4). Ignition lines were oriented perpendicular to the wind direction by design (to achieve a head fire), yet the directional semivariograms produced only negligibly different kriging outputs compared with isotropic semivariograms (Fig. 4; Table 2). The helicopter used in 2011 would have dispersed ignitions more broadly than the all-terrain vehicle (ATV) used in 2012, yet there is no evidence of this based on the semivariograms

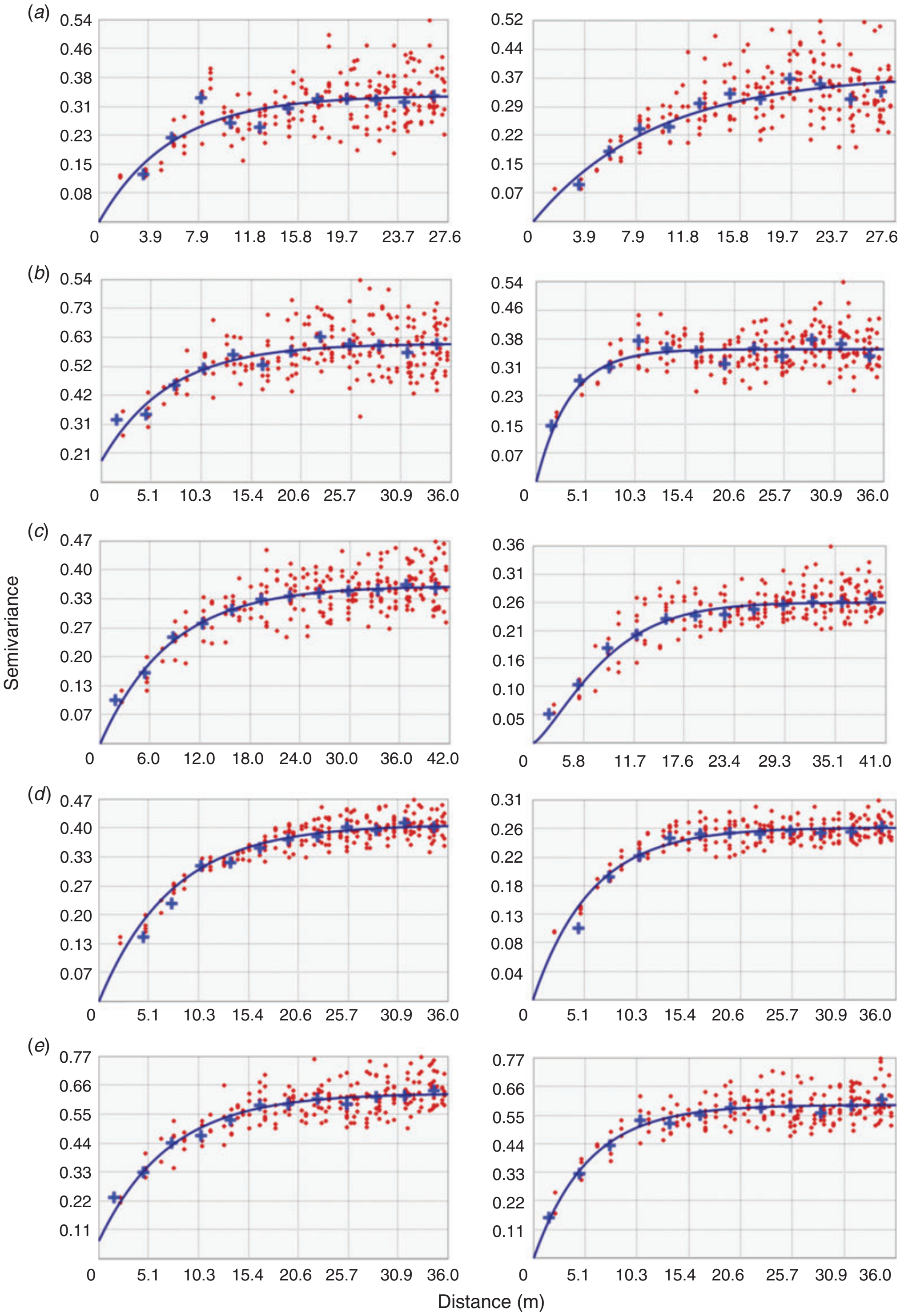

Fig. 4. Semivariograms from the ordinary kriging (OK) for both the all-pixels (left) and hottest-pixels dataset (right), for the burn blocks analysed: (*a*) 703C; (*b*) 608A; (*c*) L1G; (*d*) L2G; and (*e*) L2F. Red dots indicate binned sampled semivariances; blue line indicates fitted exponential semivariogram model; blue cross is the average value for each binned lag.

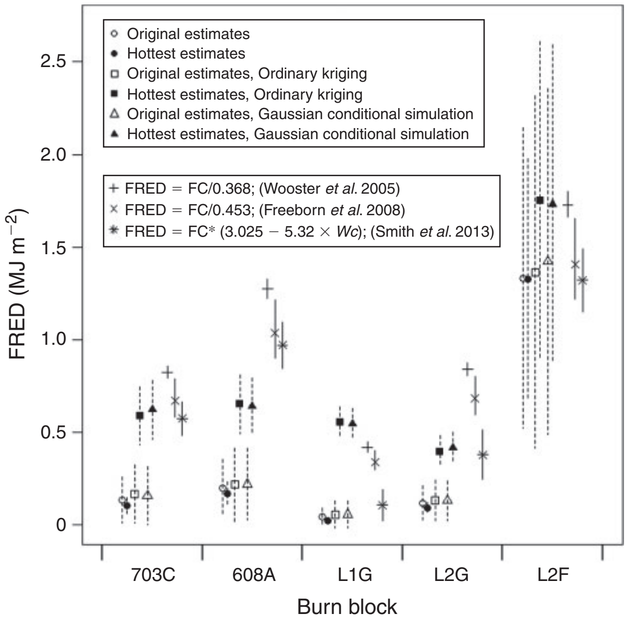

Fig. 5. Original- and hottest-pixel estimates of fire radiative energy density (FRED), before and after spatial interpolation by ordinary kriging or Gaussian conditional simulation, and compared with expectations based on observed fuel consumption (Table 1) and previously published relationships (Wooster *et al.* 2005; Freeborn *et al.* 2008; Smith *et al.* 2013). From the present study, the symbols plotted represent the means of estimated FRED and the whiskers half a standard deviation. From Wooster *et al.* (2005), Freeborn *et al.* (2008) and Smith *et al.* (2013), the symbols represent mean FRED expected based on observed fuel consumption and the coefficients shown, and the whiskers the 95% confidence intervals reported in these three papers. See Table 1 for observed fuel consumption (FC, kg m^{-2}) and gravimetric water content (*Wc*, %).

(Table 2; Fig. 4), which suggests that temporal undersampling, manifested in the WASP-derived estimates of FRED as a space for time substitution, had an overriding influence on the spatial pattern of FRED estimated from WASP.

Temporal undersampling of FRPD was caused by the ~3 min needed for the aircraft to turn around between passes, which translated into the fire being actively imaged only 15–32% of the time (Hudak *et al.* 2016*b*). Spatial undersampling of FRPD resulted because a single image frame could not always accommodate the entire active fire, especially in the larger management blocks such as 608A (Table 1). Both of these issues come into play given the practical constraints on imaging landscape-level active fires from fixed-wing aircraft.

We performed OK and GCS interpolation using all FRED estimates and only the hottest FRED estimates because the hottest pixels likely represented the least temporally and spatially undersampled (Fig. 1) and most informed WASP-derived FRED estimates (Figs 2, S1). Mean FRED values of interpolated grids were closer to expected FRED values at 703C, 608A and L2G when only the hottest pixels were included in interpolation, overcoming much of the temporal undersampling disproportionately affecting the lower estimates of FRED. The hottest-pixel interpolations still fell short of expected FRED at 608A, the largest burn block (Table 1), and thus where spatial undersampling of FRPD (Fig. 1*b*) was greatest. At L2F, the OK and GCS interpolations of the hottest pixels appear to have interpolated unrealistically high FRED estimates across sizeable fuel voids (Fig. 7, most clearly revealed where the GCS standard deviations are high), thus exceeding expected FRED on aggregation across these burn blocks (Fig. 5). GCS, like OK, preserves the mean of the input estimates in the interpolated outputs, but offers a distinct advantage over OK in that it also preserves the variance in the outputs (Berterretche *et al.* 2005), making it that much more informative (Figs 7, S3, S4).

Local accuracy of the hottest FRED pixel interpolated grids suffered relative to interpolating all the FRED estimates, as evidenced by lower correlations with field-based FRED estimates (Figs 6, S2). Our results indicate that in cases where greater local accuracy is desired, all available FRED measurements should be used for interpolation. However, FRED estimates interpolated from just the hottest pixels did not differ significantly from FRED estimated independently from ground sensors, as indicated by paired Wilcoxon-signed rank tests (Fig. 6). Therefore, under the more likely scenario where an accurate global (fire-wide) estimate of FRED is desired, it may be appropriate to subset the hottest FRED estimates before geostatistical interpolation. The lower WASP FRED estimates below ~0.2 MJ m^{-2} in the original estimates (left columns, Figs 6, S2) are piled on top of each other because of their reduced sensitivity relative to the ground sensor observations, which we consider further evidence for the undersampling problem, and added justification for excluding them for a less-biased (i.e. more accurate) global estimate, before spatial interpolation (or not) (right columns, Figs 6, S2). Fig. 5 shows how subsetting the hottest pixels to overcome FRPD undersampling bias greatly increased mean interpolated FRED at all five burn blocks, with high variation caused by many factors. On one hand, some of the cooler pixels dropped from consideration may have been sampled for peak FRPD but had little fuel to burn and release energy. On the other hand, some of the hottest pixels preserved may still underestimate FRED where fuel loads and energy release were high yet peak FRPD was missed in the sampling.

Fuel loads and subsequent fire duration varied between burn blocks. Fuel loads were lowest and sparsest in the L1G block, which had burned only 1 year previously, resulting in short fire duration, fast cooling and fewer ‘hot pixels’ of observable FRPD. Thus, there were bigger gaps to interpolate between the FRED estimates (Fig. 7), whether separated by dispersed, small patches of bare mineral soil or, much more commonly, undersampling voids. At the other extreme represented by the L2F block, the observed surface fuel loads were higher and fire duration and cooling times were longer, providing many more observations of FRPD over which to integrate a more accurate estimate of FRED. As a result, the interpolations were informed by a broader distribution of FRED estimates (Fig. 3) that were also more closely distributed in space, such that the spatial gaps between FRED estimates were narrower (Fig. 7). Hudak *et al.* (2016*b*), correcting the same five burn blocks for temporal and spatial undersampling as were considered in the present study but applying only aspatial bias corrections, also found the L2F block to be an outlier for its higher estimated FRED. This is consistent with our conclusion that L2F, having higher fuel

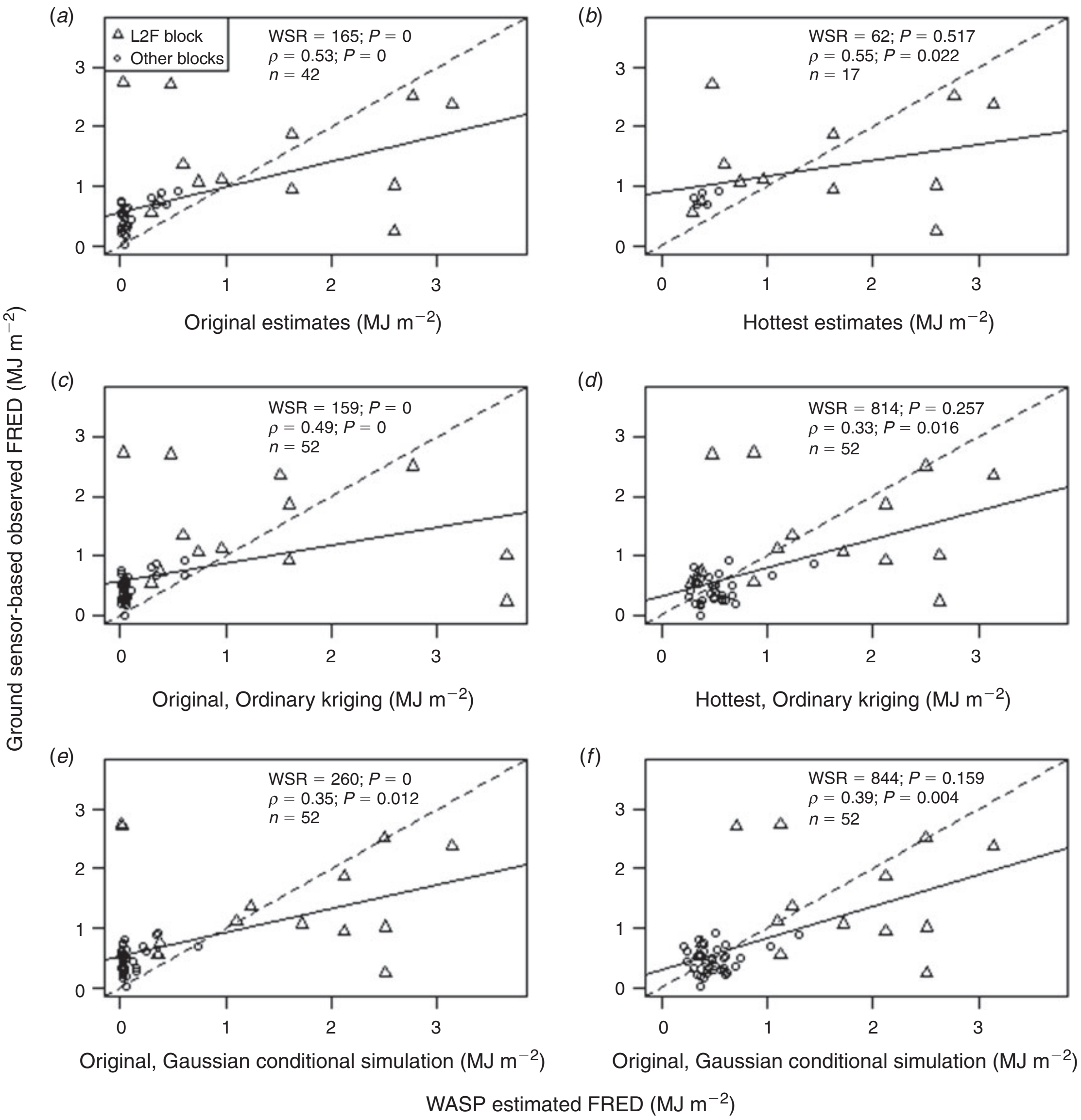

Fig. 6. Paired Wilcoxon signed-rank (WSR) test *P*-values, and Spearman rank correlations with P values, comparing image-derived fire radiative energy density (FRED) estimates (*x*-axes) with FRED integrated from 1-Hz FRPD observations at ground sensors (Dickinson and Kremens 2015; Hudak *et al.* 2016*c*). Sample sizes of original estimates and hottest estimates are lower than from the interpolated grids because of ground-based measurement locations occurring within data voids caused by undersampling. Solid lines indicate the best linear fit and dotted lines the 1 : 1 relationship.

density, consumption and fire residence time, was affected much less by undersampling than were the other four burn blocks. Therefore, we conclude that spatial interpolation was not needed and provided no real gain in the case of the L2F block.

Despite the advantages of interpolating FRED in four of our five burn blocks, the L2F block revealed a disadvantage of OK and CGS interpolation, which is that gaps between hot pixels will be filled in even when those gaps are real, and not just an artefact of the undersampling. For instance, many of the large unburned patches in the original FRED map at L2F actually did not burn, because they were areas of bare mineral soil exposed between patchy accumulations of oak leaf litter in the oak hardwoods that dominated in these vicinities. Elsewhere in L2F, needle cast from the longleaf pine overstorey created a comparatively homogeneous fuel bed more conducive to fire spread. From an operational standpoint, large areas of 'false' estimates of FRED in what are really unburned patches could be removed by passing a filter over the final kriging output, to mask out large 'smooth' patches with constant values, which could be interpreted as an artefact of geostatistical interpolation beyond the range indicated by the semivariograms (Table 2; Fig. 4). Alternatively, where the GCS standard deviation exceeds the mean (Fig. 7), or perhaps where the coefficient of variation exceeds 1, could serve as diagnostics for identifying and correcting for false positives of

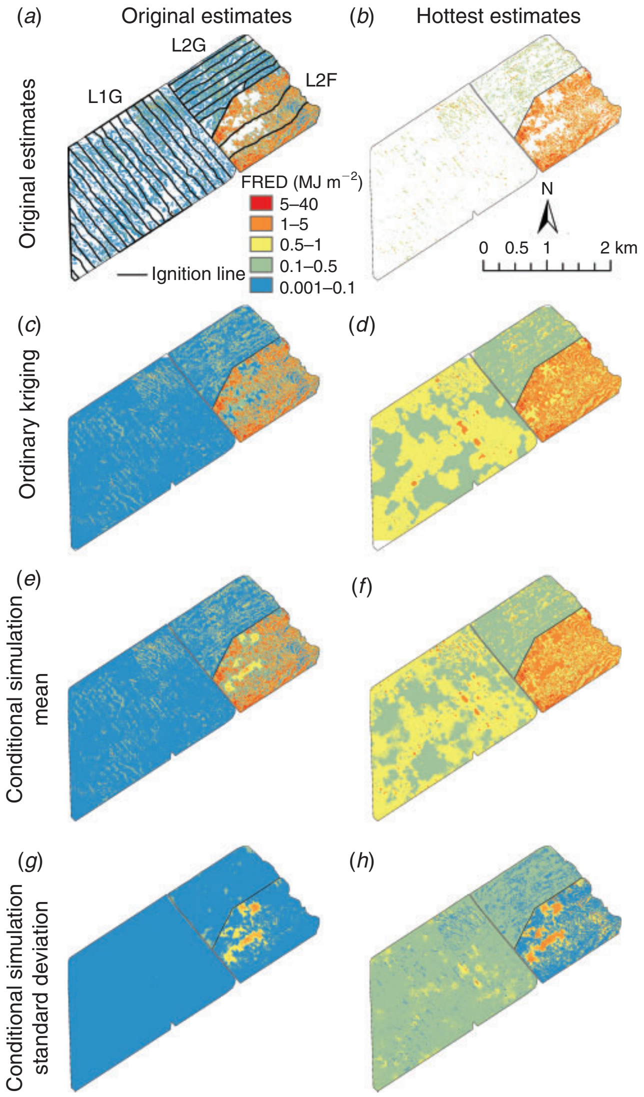

Fig. 7. Original uninterpolated (*a*, *e*), ordinary kriging (OK) interpolated (*b*, *f*), and Gaussian conditional simulation (GCS) interpolated (*c*, *d*, *g*, *h*) fire radiative energy density (FRED) maps of the 2012 burn blocks (L1G, L2G, L2F). Maps based on original FRED estimates are shown in the left column (*a*, *b*, *c*, *d*); maps based on hottest FRED estimates are shown in the right column (*e*, *f*, *g*, *h*).

FRED generated by interpolation. It is worth noting that the false positives interpolated across fuel voids in the L2F block (appearing orange in Fig. 7*d*, *h*) are magnified in the mean GCS outputs compared with the OK outputs. This is because GCS uses simple kriging, which assigns the global mean, whereas OK assigns a local mean when interpolations are outside the range of the semivariograms (Table 2; Fig. 4).

Finally, ancillary data identifying fuel presence or absence could be leveraged to increase accuracy. We tried co-kriging using as the ancillary variable pre-fire surface fuel maps predicted at 5-m resolution across these same five burn blocks from airborne lidar (Hudak *et al.* 2016*b*). Although Hudak *et al.* (2016*b*) showed the block-level means of predicted fuel loads to be accurate, local fuel heterogeneity was poorly represented, which compromised the utility of their fuel maps for co-kriging.

Conclusion

In the present study, we applied OK and GCS to maps of estimated FRED to fill in data voids produced as an artefact of temporal and spatial undersampling of FRPD from a fixed-wing aircraft. In four of five burn blocks where undersampling artefacts prevailed, we found OK and GCS to be effective and useful methods for interpolating FRED estimates across data voids, whereas in a fifth burn block (L2F) where undersampling was not so prevalent, we found that no spatial interpolation was needed. The approach as presented in this study could be applied to other similarly obtained datasets. We also encourage exploration of alternative interpolation approaches to more accurately estimate FRED in a spatially explicit manner. The FRPD images from which FRED was calculated are publicly available on the US Forest Service Research Data Archive (Hudak *et al.* 2016*a*), as are canopy cover measures and other products derived from airborne LiDAR (Hudak *et al.* 2015*b*), ground-based surface fuel (Ottmar and Restaino 2014) and FRED data (Dickinson and Kremens 2015), as well as various ancillary data layers such as ignition lines (Hudak *et al.* 2017), burn block boundaries (Hudak and Bright 2014*b*), clip-plot locations (Hudak and Bright 2014*a*), and radiometer and other ground instrument locations (Hudak *et al.* 2015*a*, 2016*c*) that can assist future analyses.

Conflicts of interest

The authors declare no conflict of interest.

Acknowledgements

This research was funded through a Postdoctoral Fellowship from the National Council of Technological and Scientific Development – CNPq via the Science Without Borders Program – Brazil (Process 208191/2014-3). Data collections and processing were possible thanks to two projects funded by the Joint Fire Science Program: the Prescribed Fire Combustion and Atmospheric Dynamics Research Experiment (RxCADRE, number 11-2-1-11) and the Fire and Smoke Model Evaluation Experiment (FASMEE, number 16–4-1–15). We thank three anonymous reviewers for their excellent comments.

References

Andreae MO (1991) Biomass burning: its history, use and distribution and its impact on environmental quality and global climate. In 'Global biomass burning: atmospheric, climatic and biospheric implications'. (Ed. JS Levine) pp. 3–21. (MIT Press: Cambridge, MA, USA)

Andriotti JLS (Ed.) (2004) 'Fundamentos de estatística e geoestatística.' (Editora Unisinos: São Leopoldo, Brazil)

Berterretche M, Hudak AT, Cohen WB, Maiersperger TK, Gower ST, Dungan J (2005) Comparison of regression and geostatistical methods for mapping leaf area index (LAI) with Landsat ETM+ data over a boreal forest. *Remote Sensing of Environment* **96**, 49–61. doi:10.1016/J.RSE.2005.01.014

Boschetti L, Roy DP (2009) Strategies for the fusion of satellite fire radiative power with burned area data for fire radiative energy derivation. *Journal of Geophysical Research* **114**, D20302. doi:10.1029/2008JD011645

Bowman DMJS, Balch JK, Artaxo P, Bond WJ, Carlson JM, Cochrane MA, D'Antonio CM, Defries RS, Doyle JC, Harrison SP, Johnston FH, Keeley JE, Krawchuk MA, Kull CA, Marston JB, Moritz MA, Prentice

IC, Roos CI, Scott AC, Swetnam TW, Van Der Werf GR, Pyne SJ (2009) Fire in the Earth system. *Science* **324**, 481–484. doi:10.1126/SCIENCE.1163886

Butler B, Teske C, Jimenez D, O'Brien J, Sopko P, Wold C, Vosburgh M, Hornsby B, Loudermilk L (2016) Observations of energy transport and rate of spreads from low-intensity fires in longleaf pine habitat – RxCADRE 2012. *International Journal of Wildland Fire* **25**, 76–89. doi:10.1071/WF14154

Cambardella CA, Moorman TB, Parkin TB, Karlen DL, Novak JM, Turco RF, Konopka AE (1994) Field-scale variability of soil properties in central Iowa soils. *Soil Science Society of America Journal* **58**, 1501–1511. doi:10.2136/SSSAJ1994.03615995005800050033X

Clements CB, Lareau N, Seto D, Contezac J, Davis B, Teske C, Zajkowski TJ, Hudak AT, Bright BC, Dickinson MB, Butler B, Jimenez D, Hiers JK (2016) Fire weather conditions and fire–atmosphere interactions observed during low-intensity prescribed fires – RxCADRE 2012. *International Journal of Wildland Fire* **25**, 90–101. doi:10.1071/WF14173

Cressie N (Ed.) (1993) 'Statistics for spatial data.' (Wiley: New York)

Dickinson MB, Kremens RL (2015) RxCADRE 2008, 2011 and 2012: radiometer data. (Forest Service Research Data Archive: Fort Collins, CO, USA)

Dickinson MB, Kremens RL (2016) Accessory publication 1: calibration procedure for single-band WASP LWIR data – incorporating spectral sensor response and atmospheric transmission. Available at http://www.publish.csiro.au/?act=view_file&file_id=WF15090_AC.pdf [Verified 17 June 2016]

Dickinson MB, Hudak AT, Zajkowski T, Loudermilk L, Schroeder W, Ellison L, Kremens RL, Holley W, Martinez O, Paxton A, Bright BC, O'Brien JJ, Hornsby B, Ichoku C, Faulring J, Gerace A, Peterson D, Mauseri J (2016) Measuring radiant emissions from entire prescribed fires with ground, airborne, and satellite sensors – RxCADRE 2012. *International Journal of Wildland Fire* **25**, 48–61. doi:10.1071/WF15090

Diggle PJ, Ribeiro PJ Jr (2007) 'Model-based geostatistics.' (Springer: New York)

Dozier J (1981) A method for satellite identification of surface temperature fields of subpixel resolution. *Remote Sensing of Environment* **11**, 221–229. doi:10.1016/0034-4257(81)90021-3

Ellicott E, Vermote E, Giglio L, Roberts G (2009) Estimating biomass consumed from fire using MODIS FRE. *Geophysical Research Letters* **36**, L13401. doi:10.1029/2009GL038581

Freeborn PH, Wooster MJ, Hao WM, Ryan CA, Nordgren BL, Baker SP, Ichoku C (2008) Relationships between energy release, fuel mass loss, and trace gas and aerosol emissions during laboratory biomass fires. *Journal of Geophysical Research – D. Atmospheres* **113**(D1), D01301. doi:10.1029/2007JD008679

Freeborn PH, Wooster MJ, Roberts G (2011) Addressing the spatiotemporal sampling design of MODIS to provide estimates of the fire radiative energy emitted from Africa. *Remote Sensing of Environment* **115**, 475–489. doi:10.1016/J.RSE.2010.09.017

Giglio L, Descloitres J, Justice CO, Kaufman YJ (2003) An enhanced contextual fire detection algorithm for MODIS. *Remote Sensing of Environment* **87**, 273–282. doi:10.1016/S0034-4257(03)00184-6

Goovaerts P (1997) 'Geostatistics for natural resources evaluation.' (Oxford University Press: New York)

Haywood A (2006) Methods for estimating distribution and abundance of blackbutt in New South Wales, Australia, from field-based samples using spatial statistics. *International Forestry Review* **8**, 329–338. doi:10.1505/IFOR.8.3.329

Hudak AT, Bright BC (2014*a*) RxCADRE 2008, 2011, and 2012: clip-plot locations. (Forest Service Research Data Archive: Fort Collins, CO, USA) Available at http://www.fs.usda.gov/rds/archive/Product/RDS-2014-0030 [Verified 17 June 2016]

Hudak AT, Bright BC (2014*b*) RxCADRE 2008, 2011, and 2012: burn blocks. (Forest Service Research Data Archive: Fort Collins, CO, USA) Available at http://www.fs.usda.gov/rds/archive/Product/RDS-2014-0031 [Verified 17 June 2016]

Hudak AT, Lefsky MA, Cohen WB, Berterretche M (2002) Integration of lidar and Landsat ETM+ data for estimating and mapping forest canopy height. *Remote Sensing of Environment* **82**, 397–416. doi:10.1016/S0034-4257(02)00056-1

Hudak AT, Bright BC, Dickinson MB, Satterberg KL (2015*a*) RxCADRE 2008, 2011, and 2012: radiometer locations. (Forest Service Research Data Archive: Fort Collins, CO, USA)

Hudak AT, Bright BC, Satterberg KL (2015*b*) RxCADRE 2008, 2011, and 2012: lidar data and derived raster products. (Forest Service Research Data Archive: Fort Collins, CO, USA)

Hudak AT, Bright BC, Kremens RL, Dickinson MB (2016*a*) RxCADRE 2011 and 2012: Wildfire Airborne Sensor Program orthorectified and calibrated long-wave infrared images. (Forest Service Research Data Archive: Fort Collins, CO, USA)

Hudak AT, Dickinson MB, Bright BC, Kremens RL, Loudermilk EL, O'Brien JJ, Hornsby BS, Ottmar RD (2016*b*) Measurements relating fire radiative energy density and surface fuel consumption – RxCADRE 2011 and 2012. *International Journal of Wildland Fire* **25**, 25–37. doi:10.1071/WF14159

Hudak AT, Dickinson MB, Rodriguez AJ, Bright BC (2016*c*) RxCADRE 2012: instrument and infrared target survey locations and attributes. (Forest Service Research Data Archive: Fort Collins, CO, USA)

Hudak AT, Bright BC, Williams BW, Hiers JK (2017) RxCADRE 2011 and 2012: ignition data. Forest Service Research Data Archive, Fort Collins. (CO, USA)

Isaaks EH, Srivastava RM (Eds) (1989) 'Applied geostatistics.' (Oxford University Press: New York)

Jacobson MZ (2001) Strong radiative heating due to the mixing state of black carbon in atmospheric aerosols. *Nature* **409**, 695–697. doi:10.1038/35055518

Journel AG (1980) The lognormal approach to predicting local distributions of selective mining unit grades. *Mathematical Geology* **12**, 285–303. doi:10.1007/BF01029417

Journel AG, Huijbregts CJ (1978) 'Mining geostatistics.' (Academic Press: London, UK)

Kaiser JW, Heil A, Andreae MO, Benedetti A, Chubarova N, Jones L, Morcrette JJ, Razinger M, Schultz MG, Suttie M, Van Der Werf GR (2012) Biomass burning emissions estimated with a global fire assimilation system based on observed fire radiative power. *Biogeosciences* **9**, 527–554. doi:10.5194/BG-9-527-2012

Kaufman YJ, Tucker CJ, Fung I (1990) Remote sensing of biomass burning in the tropics. *Journal of Geophysical Research* **95**, 9927–9939. doi:10.1029/JD095ID07P09927

Kremens RL, Dickinson MB, Bova AS (2012) Radiant flux density, energy density, and fuel consumption in mixed-oak forest surface fires. *International Journal of Wildland Fire* **21**, 722–730. doi:10.1071/WF10143

Kumar SS, Roy DP, Boschetti L, Kremens R (2011) Exploiting the power law distribution properties of satellite fire radiative power retrievals: a method to estimate fire radiative energy and biomass burned from sparse satellite observations. *Journal of Geophysical Research* **116**, D19303. doi:10.1029/2011JD015676

Mathews BJ, Strand EK, Smith AMS, Hudak AT, Dickinson MB, Kremens RL (2016) Laboratory experiments to estimate interception of infrared radiation by tree canopies. *International Journal of Wildland Fire* **25**, 1009–1014. doi:10.1071/WF16007

McKeown D, Cockburn J, Faulring J, Kremens RL, Morse D, Rhody H, Richardson M (2004) Wildfire airborne sensor program (WASP): a new wildland fire detection and mapping system. In 'Remote sensing for field users. Proceedings of the 10th Forest Service remote sensing applications conference', 5–9 April 2004, Salt Lake City, UT, USA. (Ed. JD Greer) (CD-ROM) (American Society of Photogrammetry and Remote Sensing: Bethesda, MD, USA)

Mitzenmacher M (2004) A brief history of generative models for power law and lognormal distributions. *Internet Mathematics* **1**, 226–251. doi:10.1080/15427951.2004.10129088

Montes F, Hernandez MJ, Canellas I (2005) A geostatistical approach to cork production sampling in *Quercus suber* forests. *Canadian Journal of Forest Research* **35**, 2787–2796. doi:10.1139/X05-197

Nanos N, Tadesse W, Montero G, Gil L, Alia R (2001) Spatial stochastic modeling of resin yield from pine stands. *Canadian Journal of Forest Research* **31**, 1140–1147. doi:10.1139/X01-047

O'Brien JJ, Loudermilk EL, Hornsby B, Hiers JK, Ottmar RD (2016) High-resolution infrared thermography for capturing wildland fire behaviour – RxCADRE 2012. *International Journal of Wildland Fire* **25**, 62–75. doi:10.1071/WF14165

Ononye AE, Vodacek A, Saber E (2007) Automated extraction of fire line parameters from multispectral infrared images. *Remote Sensing of Environment* **108**, 179–188. doi:10.1016/J.RSE.2006.09.029

Ordóñez C, Saavedra A, Rodríguez-Pérez JR, Castedo-Dorado F, Covián E (2012) Using model-based geostatistics to predict lightning-caused wild-fires. *Environmental Modelling & Software* **29**, 44–50. doi:10.1016/J.ENVSOFT.2011.10.004

Ottmar RD, Restaino JC (2014) 'RxCADRE 2008, 2011, and 2012: ground fuel measurements from prescribed fires.' (Forest Service Research Data Archive: Fort Collins, CO, USA)

Ottmar RD, Hiers JK, Butler B, Clements CB, Dickinson MB, Hudak AT, O'Brien JJ, Potter BE, Rowell EM, Strand TM, Zajkowski TJ (2016*a*) Measurements, datasets and preliminary results from the RxCADRE project – 2008, 2011 and 2012. *International Journal of Wildland Fire* **25**, 1–9. doi:10.1071/WF14161

Ottmar RD, Hudak AT, Prichard SJ, Wright CS, Restaino JC, Kennedy MC, Vihnanek RE (2016*b*) Pre-fire and post-fire surface fuel and cover measurements collected in the south-eastern United States for model evaluation and development – RxCADRE 2008, 2011 and 2012. *International Journal of Wildland Fire* **25**, 10–24. doi:10.1071/WF15092

Overing JD, Weeks HH, Wilson JP, Sullivan J, Ford RD (1995) 'Soil survey of Okaloosa County, Florida.' (USDA Natural Resource Conservation Service: Washington, DC, USA)

R Core Team (2015) 'R: A language and environment for statistical computing.' (R Foundation for Statistical Computing: Vienna) Available at http://www.R-project.org/ [Verified 6 May 2017]

Renard P, Straubhaar J, Caers J, Mariethoz G (2011) Conditioning facies simulations with connectivity data. *Mathematical Geosciences* **43**, 879–903. doi:10.1007/S11004-011-9363-4

Riggan PJ, Tissell RG, Lockwood RN, Brass JA, Pereira JAR, Miranda HS, Miranda AC, Campos T, Higgins RG (2004) Remote measurement of energy and carbon flux from wildfires in Brazil. *Ecological Applications* **14**, 855–872. doi:10.1890/02-5162

Roberts G, Wooster MJ (2008) Fire detection and fire characterization over Africa using Meteosat SEVIRI. *IEEE Transactions on Geoscience and Remote Sensing* **46**, 1200–1218. doi:10.1109/TGRS.2008.915751

Roberts G, Wooster MJ, Freeborn PH, Xu W (2011) Integration of geostationary FRP and polar-orbiter burned area datasets for an enhanced biomass burning inventory. *Remote Sensing of Environment* **115**, 2047–2061. doi:10.1016/J.RSE.2011.04.006

Saito H, Goovaerts P (2000) Geostatistical interpolation of positively skewed and censored data in a dioxin-contaminated site. *Environmental Science & Technology* **34**, 4228–4235. doi:10.1021/ES991450Y

Schroeder W, Oliva P, Giglio L, Csiszar IA (2014) The new VIIRS 375-m active fire detection data product: algorithm description and initial assessment. *Remote Sensing of Environment* **143**, 85–96. doi:10.1016/J.RSE.2013.12.008

Seiler W, Crutzen PJ (1980) Estimates of gross and net fluxes of carbon between the biosphere and the atmosphere from biomass burning. *Climatic Change* **2**, 207–247. doi:10.1007/BF00137988

Smith A, Tinkham WT, Roy DP, Boschetti L, Kremens RL, Kumar SS, Sparks AA, Falkowski MJ (2013) Quantification of fuel moisture effects on biomass consumed derived from fire radiative energy retrievals. *Geophysical Research Letters* **40**, 6298–6302. doi:10.1002/2013GL058232

Smith AMS, Wooster MJ (2005) Remote classification of head and backfire types from MODIS fire radiative power and smoke plume observations. *International Journal of Wildland Fire* **14**, 249–254. doi:10.1071/WF05012

Strand T, Gullet B, Urbanski S, O'Neill S, Potter B, Aurell J, Holder A, Larkin N, Moore M, Rorig M (2016) Grassland and forest understory biomass emissions from prescribed fires in south-eastern United States – RxCADRE 2012. *International Journal of Wildland Fire* **25**, 102–113. doi:10.1071/WF14166

Van Der Werf GR, Randerson JT, Collatz GJ, Giglio L (2003) Carbon emissions from fires in tropical and subtropical ecosystems. *Global Change Biology* **9**, 547–562. doi:10.1046/J.1365-2486.2003.00604.X

Wackernagel H (Ed.) (2003) 'Multivariate geostatistics. An introduction with applications.' (3rd edn) (Springer-Verlag: Berlin)

Wei X, Shao M (2009) Spatial distribution and conditional simulation of soil pH values in small watershed of loessial gully region. *Nongye Gongcheng Xuebao* **25**, 61–67.

Wooster MJ, Zhukov B, Oertel D (2003) Fire radiative energy for quantitative study of biomass burning: derivation from the BIRD experimental satellite and comparison to MODIS fire products. *Remote Sensing of Environment* **86**, 83–107. doi:10.1016/S0034-4257(03)00070-1

Wooster MJ, Roberts G, Perry GLW, Kaufman YJ (2005) Retrieval of biomass combustion rates and totals from fire radiative power observations: FRP derivation and calibration relationships between biomass consumption and fire radiative energy release. *Journal of Geophysical Research – D. Atmospheres* **110**, D24311. doi:10.1029/2005JD006318

Yamamoto JK (2005) Correcting the smoothing effect of ordinary kriging estimates. *Mathematical Geology* **37**, 69–94. doi:10.1007/S11004-005-8748-7

Yamamoto JK (2007) On unbiased back-transform of lognormal kriging estimates. *Computers & Geosciences* **11**, 219–234. doi:10.1007/S10596-007-9046-X

Yamamoto JK (2010) Back-transforming rank order kriging estimates. *Geologia-USP. Série Científica* **10**, 101–115.

Yamamoto JK, Furuie RA (2010) A survey into estimation of lognormal data. *Geociências* **29**, 5–19.

Yamamoto JK, Landim PMB (Eds) (2013) 'Geoestatística: conceitos + aplicações.' (Oficina de Texto: São Paulo, Brazil)

Zajkowski TJ, Dickinson MB, Hiers JK, Holley W, Williams BW, Paxton A, Martinez O, Walker GW (2016) Evaluation and use of remotely piloted aircraft systems for operations and research – RxCADRE 2012. *International Journal of Wildland Fire* **25**, 114–128. doi:10.1071/WF14176